Ground-Assisted Position Navigation and Timing (PNT) for Moon and Mars

Kar-Ming Cheung
Jet Propulsion Laboratory
California Institute of Technology
4800 Oak Grove Dr.
Pasadena, CA 91109
kar-ming.cheung@
jpl.nasa.gov

William W. Jun
Jet Propulsion Laboratory
California Institute of Technology
4800 Oak Grove Dr.
Pasadena, CA 91109
william.w.jun@
jpl.nasa.gov

Sriramya Bhamidipati
Jet Propulsion Laboratory
California Institute of Technology
4800 Oak Grove Dr.
Pasadena, CA 91109
sriramya.bhamidipati@
jpl.nasa.gov

Paul Carter
Jet Propulsion Laboratory
California Institute of Technology
4800 Oak Grove Dr.
Pasadena, CA 91109
paul.w.carter@
jpl.nasa.gov

Abstract— The recent exploration initiatives for robotic and human missions to the Moon and Mars require long-term communications and navigation infrastructures that provide accurate and autonomous PNT services for orbiting and surface users. NASA launched the Lunar Communication Relay and Navigation System (LCRNS) project in 2022 to meet the needs of the Artemis missions and other lunar missions. ESA, JAXA, other space agencies, and commercial entities may contribute additional lunar relay orbiters that are compatible with the NASA's orbiters via the LunaNet Interoperability Specifications.

To ensure sustained human presence at the Moon, NASA plans to deploy surface infrastructure elements that can survive the lunar nights. We are investigating the operation concept and PNT performance of augmenting the lunar relay network with a surface station with the following capabilities: 1. Provide short-range time distribution to orbiting and surface spacecraft. 2. Transmit a GNSS-like signal to augment the orbital determination (OD) schemes of lunar spacecraft for fast OD convergence. The transmitter can also act as a surface beacon that guides the lunar spacecraft during dynamic events like decent and ascent. 3. Receive lunar relay orbiter's and Earth's GPS signals and estimate corrections for orbiting spacecraft. This enables improved OD performance and accurate relative navigation of users on the lunar surface. The Joint Doppler Ranging (JDR) method requires as few as one orbiter to perform a real-time position fix of a surface user. This is particularly useful during the early stage of lunar relay network deployment when the number of orbiters is small.

The lunar surface station architecture is directly applicable to the Mars relay network, and this supports the NASA Moon-to-Mars initiative.

TABLE OF CONTENTS

1. INTRODUCTION

With the recent exploration initiatives for robotic and human missions to the Moon and Mars, it is desirable to establish a scalable orbiting and surface architecture that provides accurate and autonomous Position, Navigation, and Timing (PNT) services for orbiting and surface users at the Moon, Mars, and other planetary bodies. In this paper, we consider a ground-assisted PNT concept for lunar orbiting and surface spacecraft enabled by a lunar surface station (LSS) equipped with a high-grade frequency and timing reference. This lunar concept provides valuable insight into a future Mars-based PNT architecture.

NASA launched the Lunar Communication Relay and Navigation System (LCRNS) project in 2022 to develop long-term communications and navigation infrastructure at the Moon to meet the needs of the Artemis missions and other lunar missions. ESA, JAXA, other space agencies, and commercial entities may contribute additional lunar relay orbiters that are compatible with NASA's orbiters via the LunaNet Interoperability Specifications [1]. The lunar relay network is expected to build up incrementally starting with a few relay orbiters that focus on the lunar south pole, and to evolve to provide global coverage of the Moon. As part of PNT services, LCRNS adopts Earth's GNSS approach with orbiters broadcasting unique spread spectrum signals in S-band, and users simultaneously measuring the time-of-arrival of signals from multiple orbiters to estimate their own states.

Compared to other lunar regions, the lunar poles exhibit a unique Sun illumination environment. Due to the small 1.54º rotational obliquity, Sun illumination near the lunar poles differs considerably from other regions at lower latitude. The combination of low grazing angle of sunlight and large local topography variations results in areas that are permanently shadowed as well as regions that have continuously long illumination with only short period of darkness of just a few days [2]. The permanently shadowed regions (PSRs) are among the coldest areas on the Moon and have long been believed to harbor high concentration of volatiles including water-ice that can be harnessed for in-situ resource utilization. Thus, PSRs are prime science targets. The nearby regions with extended Sun illumination, on the other hand,

provide solar power to support surface asset operations. The temperatures near the lunar poles have been studied extensively in [3]. As an example, the temperatures at the rim of Shackleton Crater range from 75° Kelvin to 300° Kelvin, with an average of 150° Kelvin.

To ensure sustained human presence at the Moon, initially near the lunar south pole, NASA plans to deploy surface infrastructure elements that can survive the extreme temperature between lunar nights and days. For a robotic surface asset, its scientific instruments and measurement devices need to be housed in a thermally controlled vault so they can operate within acceptable temperature ranges. Therefore, a low Size, Weight, and Power (SWaP) design is highly desirable for lunar south pole operations. Solar array power and Radioisotope Thermoelectric Generator (RTG) power have been proposed to support these lunar surface assets. This includes lunar fixed or mobile surface towers that provide terrestrial communications for astronauts and rovers in the vicinity of the landing sites [4]-[6]. The same tower can be used to augment the LCRNS relay network to greatly enhance the PNT services and their performance. The LSS is envisioned to include the following PNT capabilities.

Time Distribution to Lunar Orbiting Spacecraft and Lunar Surface Station

In the human exploration era, lunar orbiting spacecraft and the LSS are expected to work collaboratively to achieve their mission goals. Given the presence of water-ice deposits, the lunar south pole is a desirable location for LSS. However, due to the Earth-Moon geometry and the long lunar night, many landing site candidates on the lunar south pole do not see Earth for an extended period in each lunar cycle. Figure 1 shows the rise and set trajectories of Earth as viewed from the Connecting Ridge. It shows that Earth spends many days below the lunar terrain.

Both the infrastructure elements, i.e., the lunar orbiting spacecraft and the LSS, need to be time-synchronized and must collectively maintain a precise globally referenced time (e.g., Earth's Universal Coordinated Time). The time reference can come from Earth's GNSS constellations [7][8] or from Earth's ground station (DSN considered in this work, which is NASA's international array of giant radio antennas that supports interplanetary spacecraft missions). In both cases, the range of transfer is quite long, of the order of 400,000 km. As compared to a fixed GNSS transmitter antenna that is of low-power and pointed towards Earth, the high-power and high-gain directional DSN transmitter that has a 34m Beam Waveguide (BWG) antenna[1] can deliver a strong and accurate timing signal to the LSS.
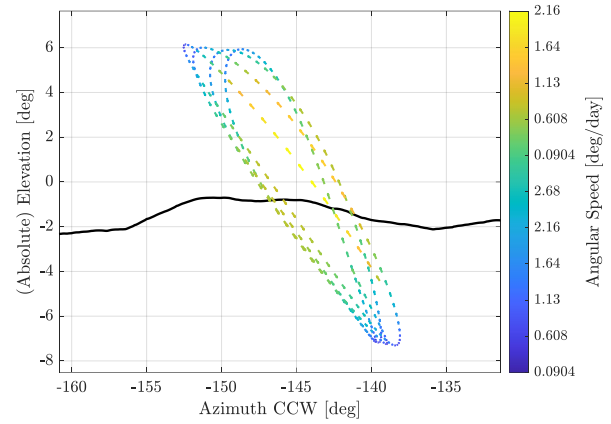
Figure 1. Earth visibility from the Connecting Ridge.

Furthermore, the LSS, likely equipped with a high-performance space clock with long-term stability, will not require frequent contact with Earth and will continue to provide accurate timing and frequency references during the long gap when Earth is below the horizon.

On the other hand, lunar orbiting spacecraft can perform an in-situ time-transfer from the LSS. The range between the LSS and the lunar orbiting spacecraft is much closer, of the order of a few thousand km or less. Given the much shorter range and higher clock stability, this serves as a worthy alternative to each lunar orbiting spacecraft independently synchronizing with Earth's ground stations.

GNSS Transmitter on Lunar Surface

Equipped with a good clock, the LSS can also broadcast a strong and stable GNSS signal to local users, and the users can measure the Doppler and range of this link as additional observables to perform OD and/or trajectory estimation. This effectively provides an additional GNSS node that is fixed on the lunar surface and acts like a pseudolite similar to Earth's GPS/GNSS applications. This approach is particularly useful to improve OD and decent trajectory estimations using Earth's GPS/GNSS signals at lunar distances [9][10].

There are many regions of interest for landing and exploration on the lunar south pole [11]. In this analysis we assume the LSS is located one of the potential sites in the Connecting Ridge at 89.45 S and 222.79 E [11] [12].

GNSS Receiver on Lunar Surface

The LSS is stationary on the lunar surface and its ephemeris is known to a high degree of accuracy. It can receive relay orbiters' and GNSS signals, broadcast range and Doppler measurements to the users, and enable the users to perform real-time position, velocity, and time (PVT) estimation relative to the station's location. This relative navigation

---

[1]DSN is equipped with a hydrogen maser as the frequency and timing reference, which is more than an order of magnitude better than the onboard GNSS Rubidium Atomic Frequency Standard (RAFS) clock in Allan deviation.

2

approach reduces some of the common measurement biases in the station link and the user link, thus providing more accurate PVT estimation.

A method that takes advantage of LSS corrections is Joint Doppler and Ranging (JDR) [13][14]. JDR is a relative navigation scheme that uses range and Doppler measurements between one or more in-situ relay orbiters, a user, and an LSS to perform real-time PVT estimation for the user relative to the nearby LSS. JDR uses both range and range-rate (Doppler) measurements by the user and the LSS. The range-rate measurements are first converted to "Doppler-derived range quantities" [15] and are then incorporated mathematically into the range measurements using the Law of Cosines (LOC). The additional Doppler observables, together with the range measurement, enable the user to perform real-time positioning with as little as one orbiter, assuming the user's altitude is known. When more orbiters are available, JDR provides additional Doppler measurements compared to range-only approaches, thus enabling higher positioning accuracy.

The JDR approach is particularly useful during the early stage of lunar relay network deployment when the number of orbiters is small. When more orbiters are available, JDR provides additional Doppler measurements compared to range-only approaches, thus enables higher positioning accuracy.

Like many Doppler-based methods, JDR is sensitive to range-rate measurement errors. Depending on the number of relay orbiters in-view there are variations of JDR that generate single-differencing and double-differencing data types to eliminate common biases in measurements. [14] provides a detailed discussion on PVT performance of the JDR as a function of the clock's characteristics.

Not only does the LSS architecture aid in-situ cislunar navigation systems such as JDR, but it is also directly applicable to the Mars relay network, and this supports the NASA Moon-to-Mars initiative [16].

The use of a LSS for navigation is not a new concept [1][17]. Previous JDR analyses include the use of a surface station that can provide differencing corrections and additional radiometric measurements [13][14]. In addition, previous literature describes the benefit of Earth-based GPS measurements for lunar navigation [9][10]. This paper introduces the use of LSS-based differential corrections to Earth-based GPS measurements at lunar distances for Cislunar users. The novel combination of these state-of-the-art navigation technologies can provide improved navigation services to users in Cislunar space with a significantly reduced navigation infrastructure.

Thus, this paper discusses multiple analyses that span over the LSS's capabilities. First, we consider choices for the high-performance clock in the LSS (Section 2). Then, we analyze time-distribution and synchronization between the DSN, LSS, and a lunar relay satellite (LRS) in a 12-hour elliptical lunar frozen orbit (ELFO) (Section 4). Next, we analyze the OD performance improvements of the LRS with Earth-based GPS measurements while also deploying the LSS as a GPS/GNSS node (Section 5). Then, we demonstrate the use of differential corrections from the LSS on Earth-based GPS measurements to aid in OD of the LRS (Section 6). Now with quantitative OD performance of the LRS, we discuss the potential performance of relative navigation for lunar surface and in-orbit users assuming the use of a 3 LRS constellation and in-situ navigation services for the lunar south pole (Section 7). Finally, we discuss the extension of the LSS concept to Mars and considerations for a Marian implementation of a surface station (Section 8).

2. EXAMPLES OF CURRENT AND UPCOMING SPACE CLOCKS

Space-based clocks or space atomic clocks provide precise timekeeping and frequency reference functions for use in outer space. These clocks are essential for space missions and satellite systems for navigation, time synchronization, and scientific purposes. Previous literature summarizes the performances and properties of some representative atomic clocks that are commercially available or are expected to be available in the upcoming future. In addition to SWaP, cost, and lifetime/reliability, a clock's short-term and long-term stabilities are important considerations in the choice of a clock for space applications. An atomic clock in space requires periodic recalibration and correction to maintain its accuracy due to various factors such as temperature fluctuations, radiation exposure, magnetic field effects, and relativistic effects of the space environment. For deployment in the LSS, these clocks must be able to maintain long-term stability with a minimal SWaP to fit within the bounds of the LSS's thermally controlled vault.

In this paper, we consider three representative high-performance clocks for deployment on the LSS, LRS constellation, and surface users: a GPS/GNSS's grade RAFS clock, the DSAC-FO clock, and low SWaP high-performance M2TIC clock.

Current GPS/GNSS's Rubidium Atomic Frequency Standard (RAFS) Clock

One of the most important aspects of GPS satellites is their onboard clock stability. The accuracy of their timing systems directly results in pseudorange measurement accuracy. Thus, GPS satellites typically employ multiple high stability clocks including RAFS clocks. For instance, the block IIF GPS spacecraft timing system includes two RAFS clocks [18].

Over the multiple generations, or blocks, of GPS satellites, the onboard clocks have evolved in performance and SWaP. The Block IIF RAFS clock has a SWaP of 9 liters, 6.3 kg, and 39 W [19] and a frequency stability of around 2.5e-15/day, and 3.5e-12 in 1 second [18][20]. The newest generation of GPS satellites, Block III, includes updated RAFS clocks with improved short-term stability (upper bound of 2e-12 / 1 second) [20]. Continuous improvements in GPS clocks and

3

updated hardware requirements for Block III satellites result in three times better pseudorange accuracy relative to previous GPS Blocks [21].

Deep Space Atomic Clock Follow-On (DSAC-FO)

Jet Propulsion Laboratory (JPL) has developed a high-performance mercury trap ion clock known as the Deep Space Atomic Clock (DSAC) to address the challenges of long-duration space missions [22]. To demonstrate the DSAC in flight, the DSAC payload was launched on June 25, 2019 aboard the Orbital Test Bed (OTB) satellite as part of the Space Test Program-2 (STP-2) mission. The mission concluded in 2021, and the onboard DSAC clock established a new record for space clock stability with a drift of 3e-16/day, which is orders of magnitude lower than other currently operating deep space clocks [22]. Its short-term stability is 1e-13 at 1 second. The DSAC clock consumes a power of 58 W, occupies a volume of 19 liters, and weights 19 kg. The SWaP is too large to be practical on a spacecraft. The DSAC-FO Technology Maturation Task (TMT) was started to mature the DSAC technology into a lower SWaP manufacturable package with the SWaP goals of 34 W, 10 kg, and to be able to fit into a GPS clock slot. In addition, the task aims to extend the clock's lifetime from 7 years to greater than 10 years. This form factor would also be easily adaptable to a 3U rack-mount package. A detailed description of the DSAC-FO development plan can be found in [23].

Low SWaP Micro Mercury Trapped Ion Clock (M2TIC)

Recently JPL has developed a number of mercury trapped ion clock prototypes with a SWaP of 1.1 liters in size, 1.2 kg in weight, and under 6 W of power [24]. This clock has a short-term stability of 5e-12 at 1 second, and a long-term stability of 1e-14. The clock's performance is independently verified by the United States Naval Research Laboratory (NRL).

There have been efforts to further reduce the SWaP of the M2TIC clock to 3 W in power and 0.7 liters in size, and to improve the reliability and lifetime. Also, the current clock prototypes use commercial-off-the-shelf quartz local oscillators which limit short-term stability. A better quartz local oscillator can be used to further improve upon the stability performance.

Choice of Clocks for Navigation Architecture

We assume the use of the DSAC-FO for the LSS's timing and frequency standard due to its superior long-term stability and relatively small SWaP. The lunar orbiting users considered in this paper also act as navigation and communication relays, requiring high-performance clocks. Thus, we assume either RAFS or DSAC-FO for lunar orbiters. Finally, surface users will likely have the most restrictions for SWaP, demanding the M2TIC.

3. LUNAR RELAY SATELLITE CONSTELLATION

In the following analyses, we assume the use of a three-satellite lunar constellation made up of LRSs in 12-hour ELFOs. Each orbiter establishes its own orbital plane 120 degrees apart. The apolunes of the orbiters maintain focus above the lunar south pole to ensure continuous access to the LSS and coverage of lunar south pole surface users. Table 1 describes the constellation's orbital elements.

Table 1. Orbital Elements of LRS Constellation

	LRS1	LRS2	LRS3
a (m)		6541.4	
e		0.6	
i (deg)		56.2	
Ω (deg)	0	120	240
ω (deg)		90	
M (deg)	0	120	240

Access Calculations with GPS Satellites

To estimate access intervals between the GPS and LRS constellations, we created a model to obtain availability of GPS signals to a lunar orbiter. Previous literature performed similar availability calculations for GPS access to lunar orbiters, utilizing GPS antenna gain patterns and flight data of received GPS signal power at high Earth orbits [25]. To mimic the results of these previously published models, we develop a surrogate model of GPS availability using simple geometric constraints.

This simple geometric access model is based on a minimum and maximum beamwidth angle from the boresight of a GPS satellite (Figure 2) where α is the half beamwidth angle of a cone originating from the GPS satellite with the boresight pointed at the center of the Earth. Although this figure demonstrates the half angles in a 2D plane, we simulate a 3D cone for access calculations. To simplify this analysis, we implement an atmospheric mask 1000 km above the surface of the Earth, resulting in a α_{min} of 15.515 deg.

Through experimentation, a maximum half beamwidth angle α_{max} of 45 degrees results in a close match to the GPS availability described in the previously published models [25]. This results in a GPS to LRS access count described in Figure 3. The figure also includes access duration and frequency of the LSS to LRS link. The LSS maintains access with the LRS for around 8 hours during each LRS orbit.

This access model is the basis for the LSS-based time distribution and navigation analyses described in the following sections.
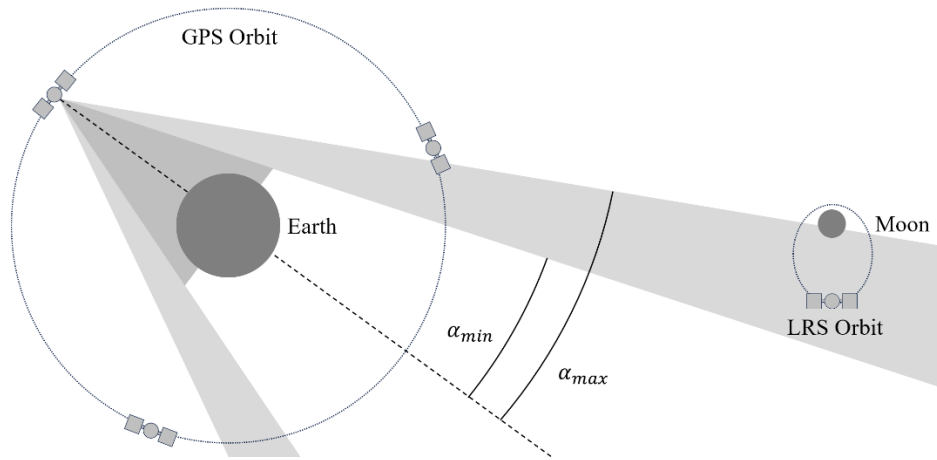
4

Figure 2. 2D geometric model of GPS availability for lunar orbiters (not to scale).
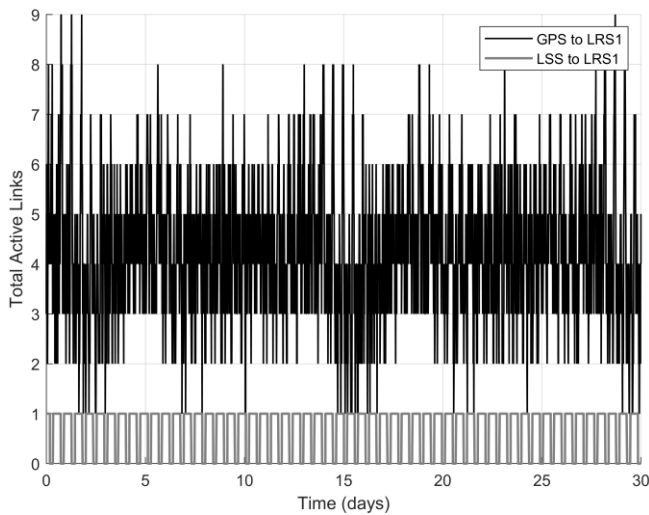

Figure 3. Access of the LRS to the GPS constellation and the LRS to the LSS.
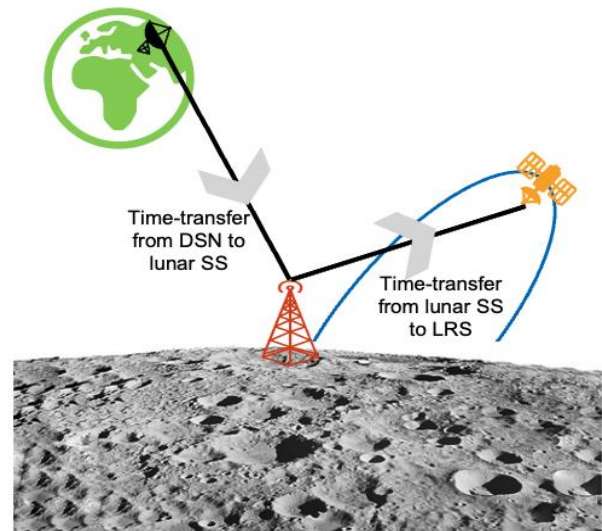**Epoch of 0 days is Jan 1 2025 00:00:000 UTC.**

Figure 4. Proposed two-prong approach of time-transfer from DSN to the LSS and then from LSS to LRS.

4. TIME-DISTRIBUTION TO LUNAR ORBITING SPACECRAFT AND LUNAR SURFACE STATION

A two-prong approach (Figure 4) is designed for time distribution from DSN to the LSS and orbiting spacecraft (lunar relay orbiters considered in this work). The two-prong approach is explained as follows:

a) firstly, when at least one DSN is in line-of-sight (LOS) with the LSS, ranging from DSN to LSS is performed. Thereafter, global transmit time and clock offset (or ranging measurement) between DSN-LSS is estimated at the DSN and then broadcast to the LSS. The LSS combines these intermittently available measurements in a Kalman filter to correct its local onsite clock, thus synchronizing it's time to that of DSN (thus, Earth's reference time).

b) secondly, to synchronize the LRS's onboard clock to that of the LSS, a two-way time-transfer is performed by the orbiter when it is in line-of-sight to the LSS. This is later utilized to estimate the orbiter's clock offset (bias and drift) with respect to the LSS.

More details regarding both these steps, and subsequent performance results will be discussed in rest of this section.

First Prong: Time-transfer between DSN-LSS

In the designed Kalman filter for the first prong, the LSS's clock corrections are estimated at each time epoch t by propagating a two-state clock vector (where subscript *SS* is taken from LSS and is representative of a surface station on the Moon): $x_{SS,t} = [b_t, \dot{b}_t]^\top$, where b_t is the clock bias state in m and $\dot{b}_t$ is the clock drift in ms^{-1}, with units converted from the timing domain through multiplication by the speed

5

of light c = 299792458 m/s. For the sake of brevity, a rundown of the standard Kalman filter expressions is not discussed in this paper. Please refer to [26] for this.

Time Update Step of Kalman Filter— To maintain the onsite clock estimate, a time update step is performed every Δt_{SS} *seconds,* based on a clock error propagation model which is modeled using the state transition matrix F_{SS} (1). The associated process noise covariance $Q_{SS}(\Delta t_{SS})$ (2) is defined in terms of the power spectral density (PSD) coefficients h_0, h_{-1}, h_{-2} from an Allan deviation plot for the clock [27][28]. These PSD coefficients reflect the short-term and long-term stability of the LSS's onsite clock. The output from this step is the predicted state estimate $\bar{x}_{SS,t} = \left[\bar{b}_t, \dot{\bar{b}}_t\right]^\top$ and the associated state covariance $\bar{P}_{SS,t}$.

$$F_{LSS} = \begin{bmatrix} 1 & \Delta t_{SS} \\ 0 & 1 \end{bmatrix} \qquad (1)$$

$$Q_{SS}(\Delta t) = \begin{bmatrix} \frac{h_0}{2}\Delta t + 2h_{-1}\Delta t^2 + \frac{2}{3}\pi^2 h_{-2}\Delta t^3 & h_{-1}\Delta t + \pi^2 h_{-2}\Delta t^2 \\ h_{-1}\Delta t + \pi^2 h_{-2}\Delta t^2 & \frac{h_0}{2\Delta t} + 4h_{-1} + \frac{8}{3}\pi^2 h_{-2}\Delta t \end{bmatrix} \quad (2)$$

Measurement Update Step of Kalman Filter— When DSN is in line-of-sight with the LSS, a two-way ranging protocol is initiated between DSN and the LSS [28]. In this, DSN measures the round-trip phase delay of a ranging signal exchanged to estimate the ranging between DSN and LSS $r_{SS,n-1}^{DSN}$ at frame $(n-1)$: a carrier signal is sent from DSN at transmit time $T_{tx,n-1}^{DSN}$ that is received at the LSS at local time $T_{rx,n-1}^{SS}$ and then again transmitted from the LSS at local time $T_{tx,n-1}^{SS}$ that is received back again at the DSN at $T_{rx,n-1}^{DSN}$. Leveraging the times $T_{tx,n-1}^{SS}$ and $T_{rx,n}^{DSN}$ and ranging measurement $r_{SS,n-1}^{DSN}$, an estimate of the LSS's clock bias $b_{SS,n-1}^{DSN}$ is also estimated. Executing a second round of two-way ranging protocol at frame n, another estimate of ranging between DSN and LSS $r_{SS,n}^{DSN}$ and thereafter, LSS's clock bias $b_{SS,n}^{DSN}$ are estimated. The latest ranging measurement $r_{SS,n}^{DSN}$ along with DSN's estimate of the LSS's clock bias $b_{SS,n}^{DSN}$ and clock drift $\dot{b}_{SS,n}^{DSN}$ (calculated as $\left(b_{SS,n}^{DSN} - b_{SS,n-1}^{DSN}\right)/(T_{rx,n}^{DSN} - T_{rx,n-1}^{DSN})$ are uplinked to the LSS along with the DSN transmit time $T_{tx,n+1}^{DSN}$.

Note that, for this work, both DSN times (i.e., $T_{tx,n-1}^{DSN}$ and $T_{rx,n-1}^{DSN}$) and LSS's local times (i.e., $T_{rx,n-1}^{SS}$ and $T_{tx,n-1}^{SS}$) are considered to be logged in the Earth's reference time (e.g., Coordinated Universal Time). There are ongoing research studies on the use of a separate lunar reference time by lunar assets, which is fully independent of Earth's reference time. Our approach is still generalizable to work under such setup, however, it would require DSN stations to have access to a precise estimate of the offset between the lunar reference and Earth's reference time, and going into further details regarding this is beyond the scope of this paper.

When a message broadcast from DSN is received at the LSS at local time $T_{LSS,t}$, a measurement update step is performed to estimate the updated state estimate $\hat{x}_{SS,t}$ and the associated state covariance $\hat{P}_{SS,t}$. The measurement $z_{SS,t}$ (3) is formulated by extrapolating the DSN-estimated clock bias using the predicted clock drift estimate from time update step seen earlier. This measurement provides an estimate of the LSS's onsite clock bias and drift. The measurement model is a 2x2 identity matrix.

$$z_{SS,t} = \begin{bmatrix} b_{SS,n}^{DSN} + \bar{\dot{b}}_t \, (1/c) \, r_{SS,n}^{DSN} \\ \dot{b}_{SS,n}^{DSN} \end{bmatrix} \qquad (3)$$

For this work, we consider an assumption that the ranging measurement did not change significantly between two DSN uplinks, i.e., $r_{SS,n}^{DSN} = r_{SS,n+1}^{DSN}$. The measurement noise covariance matrix $R_{SS} = diag(\sigma_1^2, \sigma_2^2)$, where σ_1^2, σ_2^2 are hyperparameters tuned based on signal-in-space errors.

Second Prong: Time-transfer between LSS-orbiter

Our formulation for two-way timing exchange protocol between the LSS and LRS is inspired by the derivation described in [29][30]. During frame $(m-1)$, a transmission from the LRS at time $T_{tx,m-1}^{LRS}$, will be received at the LSS at time $T_{rx,m-1}^{SS}$, after which a transmission sent from LSS at time $T_{tx,m-1}^{SS}$ is received at the LSS at time $T_{rx,m-1}^{SS}$.

In the Kalman filter designed for the second prong, the LRS's clock corrections are estimated at each time epoch t by propagating a four-state clock vector: $x_{LRS,t} = [\tau_t, \dot{\tau}_t, \gamma_t, \dot{\gamma}_t]^\top$, where τ_t is the clock bias state in m and $\dot{\tau}_t$ is the clock drift in ms^{-1}, γ_t is the relative time-of-flight (TOF) state in m and $\dot{\tau}_t$ is the drift associated with relative TOF state in ms^{-1}.

A time update step is executed at LRS every Δt_{LRS} *seconds*, wherein the state transition matrix F_{SS} is as follows:

$$F_{LSS} = \begin{bmatrix} 1 & \Delta t_{LRS} & 0 & 0 \\ 0 & 1 & 0 & 0 \\ 0 & 0 & 1 & \Delta t_{LRS} \\ 0 & 0 & 0 & 1 \end{bmatrix} \qquad (4)$$

The process noise covariance model Q_{SS} models process noise as a zero-mean multivariate normal distribution with $Q_{LRO} = diag(Q_\tau, Q_\gamma)$ where Q_τ is modeled as $Q_\tau = Q_{SS}(\Delta t_{LRO})$ (2). The second component of the process noise covariance matrix Q_γ is modeled as:

$$Q_\gamma = \begin{bmatrix} \frac{1}{2}\sigma_\gamma^2 \Delta t_{LRS}^2 & \sigma_\gamma^2 \Delta t_{LRS} \\ \sigma_\gamma^2 \Delta t_{LRS} & \sigma_\gamma^2 \Delta t^2 \end{bmatrix} \qquad (5)$$
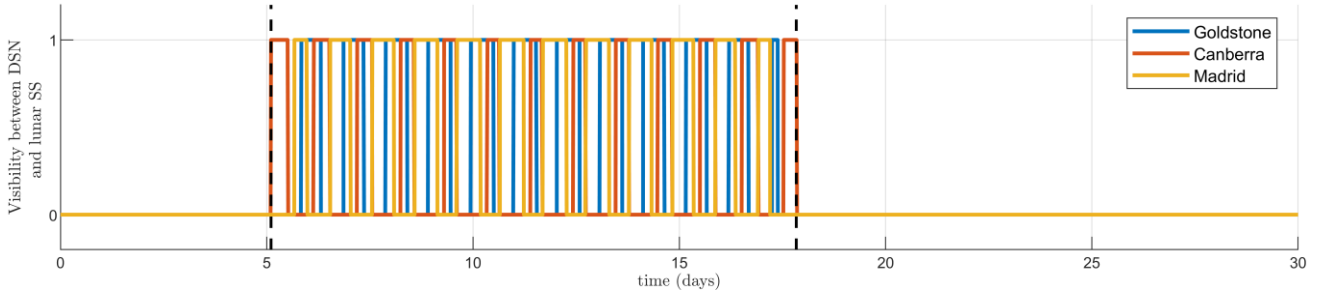
6

Figure 5. DSN station visibility at the LSS wherein the window between the two dotted black lines is considered for validation of the first-prong. Note that, across the 30 days, before 5th day and from 18th day onwards Earth is below lunar terrain (as discussed earlier in Section 1), hence none of the DSN stations are visible.

where $\sigma_{\dot{\gamma}}^2$ is the variance in relative radial velocity between Earth's ground station and the LSS, which depends on perturbations induced by Earth's and Moon's rotations as well as errors in frame transformations.

The output from this time update step is the predicted state estimate $\bar{x}_{LRS,t}$ and the associated state covariance $\bar{P}_{LRS,t}$.

The measurement update step is executed when the LRS has line-of-sight to the LSS and after the completion of one round of two-way ranging. In the measurement update step, the updated state estimate is $\hat{x}_{LRS,t}$ and the associated state covariance is $\hat{P}_{LRS,t}$. The measurement vector $z_{LRS,t}$ (6) is formulated based on the transmit and receive times at the LSS and the LRS. The measurement model H_{LRS} is shown in (7).

$$z_{LRS,t} = \begin{bmatrix} T_{rx,m-1}^{SS} - T_{tx,m-1}^{LRS} \\ T_{rx,m-1}^{LRS} - T_{tx,m-1}^{SS} \end{bmatrix} \quad (6)$$

$$H_{LRS} = \begin{bmatrix} -1 & 0 & 1 & 0 \\ 1 & 0 & 1 & 0 \end{bmatrix} \quad (7)$$

The measurement noise covariance matrix $R_{LRS} = diag(\sigma_{LRS,rx}^2, \sigma_{SS,rx}^2)$, where the variances $\sigma_{LRS,rx}^2$ and $\sigma_{SS,rx}^2$ are associated with the time-of-arrival estimator and antenna characteristics at the LRS and the LSS, respectively.

Modeling and Simulation Setup

DSN details— The three ground stations in the DSN [31][32] are as follows: a) the Goldstone Deep Space Communications Complex (35°25'36" N, 116°53'24" W); b) the Madrid Deep Space Communications Complex (40°25'53" N, 4°14'53" W); and c) the Canberra Deep Space Communication Complex in the Australian Capital Territory (35°24'05" S, 148°58'54 E). When more than one DSN is in line-of-sight with the LSS, one DSN is randomly picked to engage with the LSS.

Clocks at LSS and LRS— A sensitivity analysis is performed by evaluating the time-distribution performance at the LSS using two different onsite clocks: a) DSAC-FO (taken from [7]): time deviation is $4e^{-11}$ and the PSD coefficients are $h_0 = 1.8e^{-27}, h_{-1} = 0, h_{-2} = 0$; and b) M2TIC clock (estimated from [24]): time deviation is $1.5e^{-9}$ and the PSD coefficients are $h_0 = 1.45e^{-22}, h_{-1} = 0, h_{-2} = 0$. Similarly, the time-transfer performance at the LRS is evaluated using

two different onboard clocks: a) DSAC-FO; and b) RAFS (taken from [7]): time deviation is $4.8e^{-9}$ and the PSD coefficients are $h_0 = 0.8e^{-23}, h_{-1} = 0, h_{-2} = 0$. The measurement noise covariances are modeled to be an order of magnitude higher than the process noise covariances.

Analysis and Results

A simulation start time of January 1, 2025 12:00 AM UTC and duration of 30 days is considered for validating our approach. Figure 5 demonstrates the variation in the visibility of the three DSN stations as viewed from the LSS (with a masking angle of 10 deg). Overall, the percentage of time that a visibility link exists between DSN and the LSS is 41.19%, which is consistent with the phenomenon explained earlier in Figure 1. For analysis of the first-prong, a shortened window highlighted by the dashed black lines is considered where the percentage of time for which at least one DSN is in line of sight with the LSS is 96.91%.

Figure 6 demonstrates the accuracy of the first-prong approach, wherein the upper plot showcases the error in estimated clock bias at the LSS (shown in blue) while the lower plot focuses on the error in estimated clock drift (shown in blue). The $\Delta t_{SS} = 60\ s$. In these plots, the red dashed lines indicate the lower and upper 1-σ bounds extracted from the estimated state covariance in the Kalman filter. The area highlighted in lavender (bound by vertical black lines) are indicative of the regions where no DSN visibility exists. Over this desired window, the clock corrections are successfully estimated with an accuracy of $1.5e^{-3}$ μs Root-Mean-Square (RMS) in bias and $7.3e^{-5}$ ns/s RMS in drift. This validates that the proposed method can maintain nano-second-level accuracy over the entire desired window while also efficiently handling short durations of no DSN visibility. Other quantitative statistics related to DSAC-FO and M2TIC are discussed in Table 2, where our proposed technique with an onboard DSAC-FO achieves nanosecond and an onboard M2TIC achieves microsecond-level clock accuracy.

Note that analyzing the segments where no DSN visibility exists for long periods of time is beyond the scope of this paper. This is because the clock characteristics in these segments governed by its long-term stability for which there exists a wide variety of dedicated literature.
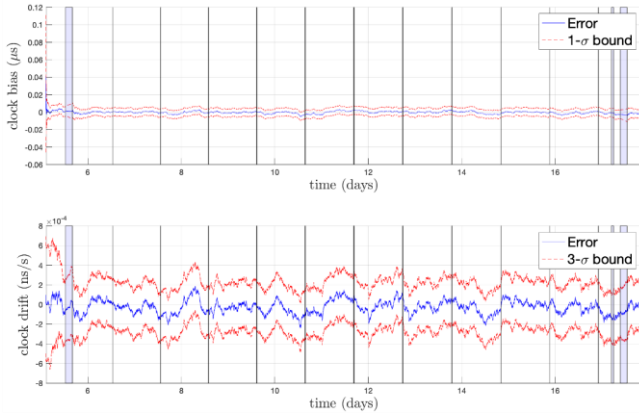
7

Figure 6. Error in clock estimates at the LSS with an onsite DSAC-FO (first-prong).

Table 2. Quantitative Statistics Associated with Error in Clock Bias and Drift for DSAC-FO and M2TIC in First-Prong (i.e., at the LSS with aiding from DSN stations)

Metrics	DSAC-FO		M2TIC	
	Clock Bias (μs)	Clock Drift (ns/s)	Clock Bias (μs)	Clock Drift (ns/s)
Mean	$1.1e^{-3}$	$5.9e^{-5}$	$3.3e^{-1}$	$1.6e^{-2}$
RMS	$1.5e^{-3}$	$7.3e^{-5}$	$4.2e^{-1}$	$2.0e^{-2}$
95%	$2.7e^{-3}$	$14.1e^{-5}$	$7.9e^{-1}$	$4.0e^{-2}$

To validate the second-prong, the estimated clock accuracies are analyzed for a shorter time window between $1193820\ s$ and $1204620\ s$ (during which LRSs have visibility with the LSS). For the sake of brevity, only results pertaining to LRS-1 are discussed, similar performance observed for other LRSs as well. Figure 7 demonstrates the accuracy of the clock estimates (first two states of $x_{LRS,t}$) at LRS-1 (with an onboard RAFS clock) with the upper plot showcasing bias error (shown in blue) and lower plot showcasing drift error (shown in blue). The $\Delta t_{LRS} = 60\ s$. Furthermore, Figure 8 demonstrates the accuracy of the last two states of $x_{LRS,t}$ with the upper plot showcasing the error in relative TOF between LSS and LRS-1 (shown in blue) and lower plot showcasing the associated drift error (shown in blue). The red dotted lines in Figures 7 and 8 indicate the lower and upper 1-σ bounds derived from the estimated state covariance in the Kalman filter. Given the highly elliptical nature of ELFO considered for LRS-1, simultaneously estimating the relative TOF and clock states aid in maintaining nanosecond-level accuracy at the LRS-1. Over the entire window, the clock corrections are estimated with a high accuracy of $4.3e^{-3}\ \mu$s Root-Mean-Square (RMS) in bias and $2.1e^{-3}\ n$s/s RMS in drift.

Table 3 lists the quantitative statistics for error in estimated LRS-1 states for two cases, i.e., one with an onboard RAFS
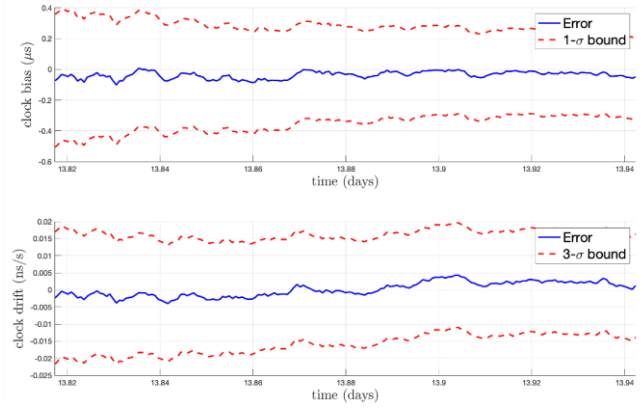
Figure 7. Error in clock estimates at LRS-1 with an onboard RAFS at LRS-1 and DSAC-FO at the LSS (second-prong).
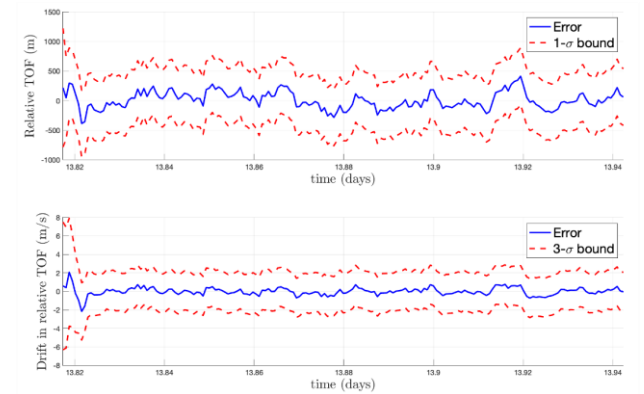
Figure 8. Error in relative time-of-flight between LRS-1 and LSS with an onboard RAFS at LRS (second-prong).

Table 3. Quantitative Statistics for Error in Estimated LRS States with RAFS Onboard LRS (LSS has DSAC-FO)

Clock type	Metrics	Clock Bias (μs)	Clock Drift (ns/s)	Rel. TOF (m)	Rel. TOF rate (m/s)
RAFS	Mean	$3.7e^{-2}$	$1.8e^{-3}$	116.1	0.3
	RMS	$4.3e^{-2}$	$2.1e^{-3}$	144.2	0.4
	95%	$7.6e^{-2}$	$3.6e^{-3}$	277.7	0.7
DSAC-FO	Mean	$0.3e^{-3}$	$0.1e^{-4}$	3.1	0.1
	RMS	$0.1e^{-3}$	$0.1e^{-4}$	3.8	0.1
	95%	$0.7e^{-3}$	$0.1e^{-4}$	7.8	0.2

and the other with a DSAC-FO. This successfully validates that the proposed two-prong approach of time-transfer to LRS (first from DSN to LSS and then from LSS to LRS) can maintain nano-second level accuracy onboard LRS.

8

5. GNSS TRANSMITTER ON THE LUNAR SURFACE

An additional navigation signal originating from the lunar surface can improve orbit determination with Earth-based GPS signals for lunar orbiters. This section analyzes the use of an LSS on the lunar south pole that can broadcast navigation signals and relay communications to an LRS constellation. This not only provides an additional range measurement for LRS OD, but also adds valuable diversity in geometry for the trilateration solution of the orbiter. The LSS also acts as a communications hub for nearby surface users. These surface users can take advantage of the LSS navigation broadcasts for surface positioning.

Transmitting Frequency of LSS GPS Transmitter

Because the LRS is significantly closer to the LSS than the GPS constellation, we must carefully consider the LSS GPS transmitter frequency and power to prevent potential interference. If the LSS transmits near the standard GPS L-band, a user may only require two antennas to one central GPS radio. However, additional complications arise with the LRS's large variance in range from the LSS, resulting in a variance in received signal power. If the LSS transmits a GPS signal at S-band, interference is no longer an issue, but the LRS now may require two radios. This analysis performs a simplified link budget to gauge the range in received power from GPS to the LRS and from the LSS to the LRS and to compare the use of L1 or S-band as the LSS's transmit frequency.

Link Budget– The effective isotropic radiated power (EIRP) of GPS satellites is approximately 29 dBW [25][33]. Assuming a receiver antenna gain of 3 dBi for an Earth-based surface user, a transmitting frequency at L1 (1575.42 MHz), and a 20,200 km free space path loss (FSPL), the received power on the Earth's surface is -150.5 dBW which is within the requirement for GPS received signal power [34] (Table 4). Repeating the simplified link analysis with the LRS requires assumptions on the receiving antenna of the LRS. This report approximates the LRS receiver antenna gain with a 50 cm antenna designed for Earth-based GPS measurements by the Lunar Gateway [25]. Assuming the LSS transmits at L1 and a 60% antenna efficiency for the LRS, the following equation calculates the antenna gain:

$$G_r = 10 \log_{10}\left(\frac{4\pi\eta A}{\lambda^2}\right) \qquad (8)$$

where η is the antenna efficiency, A is the antenna area, and λ is the received signal wavelength. Knowing the minimum and maximum range between the GPS satellites and the LRS, we calculate the FSPL with:

$$L_{FSPL} = 20 \log_{10}(d) + 20 \log_{10}(f) + 20 \log_{10}\left(\frac{4\pi}{c}\right) \qquad (9)$$

where d is the distance travelled by the radio signal, f is the transmitting frequency, and c is the speed of light in vacuum. Table 4 describes the minimum and maximum received signal power to the LRS from Earth-based GPS signals.

To ensure that the received power of the LSS's broadcasted signal is close to the power of the GPS signal, this analysis assumes a reduced transmitting EIRP for the LSS (Table 4). Due to the highly elliptical orbit of the LRS, the range between the LSS and LRS varies significantly: from 5639 km to 9037 km. These minimum and maximum ranges only account for intervals of access between the LRS and LSS and assume a 15 deg elevation mask on the LSS. This difference in range results in a 4.1 dB difference in FSPL and received power. Although a space-rated GPS receiver can accommodate a 4.1 dB difference in received power, the L-band transmission can still interfere with low lunar orbiters (LLO) passing through the beamwidth of the LSS. A LLO at 200 km above the lunar south pole that is also performing OD with Earth-based GPS measurements would receive L-band signals from the LSS at 30 dB higher received power, resulting in interference. Surface users nearby the LSS may not be significantly affected by the LSS L-band broadcast assuming the LSS gain drops off in the 15-degree elevation mask. Thus, we instead assume the LSS transmits GPS pseudorandom noise (PRN) codes at S-band.

Repeating this link analysis assuming the LSS transmits at S-band (2.5 GHz) results in a similar range of received power, but with a smaller chance of interference (Table 5). To further reduce the maximum difference in received power, one can

Table 4. Link Budgets for Minimum and Maximum Range between GPS to Earth Surface, GPS to LRS, and LSS to LRS at L1

	GPS to Earth Surface	GPS to LRS		LSS to LRS	
		Minimum Range	Maximum Range	Minimum Range	Maximum Range
Transmit EIRP (dBW)	29.0	29.0		-6.1	
FSPL @ L1 (dB)	-182.5 (20,200 km)	-208.4 (398,862 km)	-208.8 (414,796 km)	-171.4 (5639 km)	-175.5 (9037 km)
Receiver Antenna Gain (dBi)	3.0	16.1		16.1	
Received Power (dBW)	-150.5	-163.3	-163.6	-161.4	-165.5
Maximum Difference in Received Power (dBW)	N/A	0.3		4.1	

9

Table 5. Link Budgets for Minimum and Maximum Range between LSS to LRS and LSS to LRS with Custom Antenna at S-Band (2.5 GHz)

	LSS to LRS		LSS to LRS Custom LSS Antenna Gain	
	Minimum Range	Maximum Range	Minimum Range	Maximum Range
Transmit EIRP (dBW)	-6.1		-8.0	-4.2
FSPL @ S-Band (dB)	-175.4 (5639 km)	-179.5 (9037 km)	-175.4 (5639 km)	-179.5 (9037 km)
Receiver Antenna Gain (dBi)	20.1		20.1	
Received Power (dBW)	-161.4	-165.5	-163.3	-163.6
Maximum Difference in Received Power (dBW)	4.1		0.3	

design the LSS transmitting antenna gain pattern to drop off as a function of angle from boresight. We assume that the target maximum difference in received power for the LRS in S-band is 0.3 dB. Depending on radio design, this custom gain pattern limits the usability of the LSS as a navigation beacon to only the LRS orbit. At 75 degrees from boresight the LSS can begin access with the LRS. At this elevation, the LSS transmit EIRP can be -8.0 dBW. Near the boresight of the LSS antenna, the transmit EIRP can increase to -4.2 dBW to counteract losses due to FSPL (Table 5).

From this basic link analysis, we determine that the LSS should transmit its navigation signal at S-band. A custom antenna gain pattern can maintain a 0.3 dB maximum difference in received power for the LRS throughout its orbit.

The LSS also communicates and broadcasts a ranging code to nearby surface users. However, we assume this surface-to-surface broadcast is on a separate UHF band instead of S-band. For surface user positioning, the LRS constellation will act as the navigation constellation and broadcast ranging codes down to the lunar south pole surface. The navigation constellation will adjust their transmit power to ensure the received power at the surface is near constant.

Geometry Improvements with an LSS GNSS Transmitter

Geometry is a large problem during trilateration when using Earth-based GPS signals at lunar distances. The addition of a GPS signal from the LSS improves the geometry of the trilateration significantly. This analysis demonstrates the improvements in dilution of precision (DOP) resulting from a GPS broadcast from the LSS to the LRS.

DOP With LSS Broadcast– If the LSS can broadcast a navigation code in S-band to the LRS, it can provide another range measurement that aids in the trilateration geometry. To analyze the change in trilateration geometry, we first calculate the dilution of precision (DOP) of the LRS with GPS measurements. When the LRS can see four or more satellites with the surrogate model of GPS availability, the simulation calculates the geometric DOP (GDOP), position DOP (PDOP), and time DOP (TDOP). Figure 9 describes the GDOP and PDOP of the LRS with and without the LSS as a navigation node. No DOP value is displayed when the
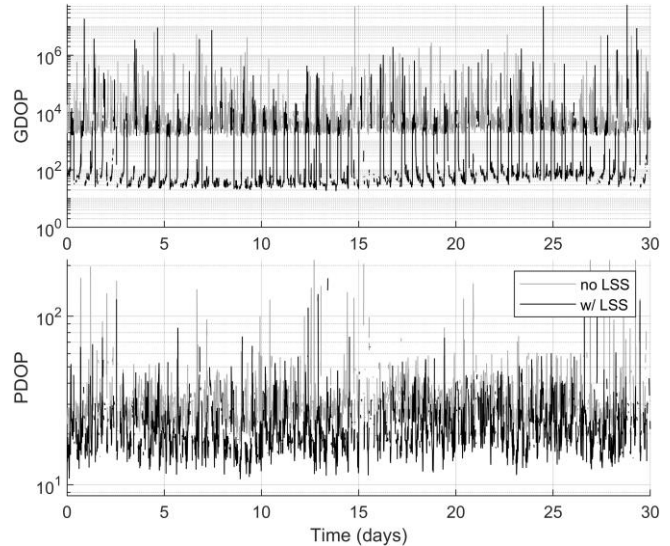
Figure 9. DOP of the LRS with GPS and LSS. GDOP and TDOP are nearly identical; they differ by 5e-4%.

number of satellites in view is under three for PDOP and four for GDOP.

When the LSS is in view and transmitting measurements to the LRS, the GDOP and TDOP improve by around two orders of magnitude. PDOP improves by 37% on average throughout a 30-day period. The addition of the LSS as a navigation node for trilateration of the LRS provides significant benefits to the geometry of orbit determination and time synchronization.

Onboard Orbit Determination of LRS with LSS Broadcast

Now that we have pseudorange measurements from GPS and the LSS, we can attempt OD of the LRS. This analysis assumes that the LRS estimates its position, velocity, and clock bias at a given epoch with measurements taken over time and processed by a batch estimator.

The measurements used for orbit determination in this analysis include GPS-based and LSS-based pseudorange measurements. A realistic implementation of onboard OD for the LRS would likely include the use of other navigation

10

techniques such as cross-link measurements [35] and optical navigation [36]. However, this analysis only utilizes GPS-based and LSS-based pseudorange measurements to gauge the achievable performance of these systems.

Measurement Models– During trilateration, the LRS receives pseudorange measurements from the GPS constellation and the LSS. These pseudorange measurements include a bias due to the LRS's clock bias:

$$h_k(\bar{X}) = \rho_k + c\Delta t_k$$
$$= \sqrt{(x_k - S_{x,k})^2 + (y_k - S_{y,k})^2 + (z_k - S_{z,k})^2} \quad (10)$$
$$+ c\Delta t_k$$

where $h_k(\bar{X})$ is the measurement model of the estimated state $\bar{X}$ at instance k, ρ is the range between the transmitting satellite's position and the user's position, c is the speed of light in vacuum, and Δt is the user's estimated clock bias. $[x \quad y \quad z]^T$ and $[S_x \quad S_y \quad S_z]^T$ are the user's and transmitting satellite's three-element inertial, cartesian position, respectively. As with GPS, there are a few assumptions embedded into this measurement model: 1) the transmitting GPS satellites all have well-synchronized clocks and 2) residual biases that exist on the satellite clocks are modeled and broadcast to the user. In this case, the LSS also performs a time synchronization with the DSN to synchronize with GPS time before starting navigation services. The LSS can similarly model and broadcast an estimate of the LSS clock bias to the LRS. The GPS and LSS clock models are not perfect, however, so this analysis also simulates clock modeling errors on all transmitting nodes.

Batch Least Squares Processor– The batch least squares method processes a single "batch" of data instead of individual measurements over time. This results in superior estimation performance compared to sequential filters but requires more computational resources to run in real-time [37]. The batch processor accumulates measurements throughout an analysis period and calculates a new state estimate at a given epoch. Unlike sequential filters, this measurement accumulation process repeats until the state estimate converges. The batch processor measurement accumulation is described through the following equations [38]:

$$\tilde{H}_k = \left[\frac{\partial G(\bar{X}, t_k)}{\partial \bar{X}}\right]^* \quad (11)$$

$$y_k = Y_k - G(\bar{X}_k^*, t_k) \quad (12)$$

$$H_k = \tilde{H}_k \Phi(t_k, t_0) \quad (13)$$

$$H = [H_1^T \ H_2^T \ ... \ H_n^T]^T \quad (14)$$

$$y = [y_1^T \ y_2^T \ ... \ y_n^T]^T \quad (15)$$

where $G(\bar{X}, t_k)$ is the measurement model at the estimated state $\bar{X}$ and time t_k, Y_k is the observation vector, $\Phi(t_k, t_0)$ is the state transition matrix, and the symbol $*$ represents an evaluation on the nominal trajectory [38]. One can solve for the state estimate error with R as the measurement noise covariance:

$$\bar{X}_0 = (H^T R^{-1} H)^{-1} H^T R^{-1} y \quad (16)$$

If the state estimate error is larger than a given convergence threshold, the measurement accumulation process repeats with the updated epoch state estimate and resultant nominal trajectory.

This simulation's estimated state $\bar{X}_k$ includes the LRS position, velocity, and clock bias at a certain epoch k:

$$\bar{X}_k = [x_k \quad y_k \quad z_k \quad v_{x,k} \quad v_{y,k} \quad v_{z,k} \quad c\Delta t_k]^T$$

Once the LRS's position and velocity state is known at an epoch, the orbiter can propagate its orbit using a simple two-body dynamics model:

$$\dot{\bar{X}}_k = F(\bar{X}_k, t_k)$$
$$= \left[v_{x,k} \quad v_{y,k} \quad v_{z,k} \quad -\frac{\mu x_k}{r_k^3} \quad -\frac{\mu y_k}{r_k^3} \quad -\frac{\mu z_k}{r_k^3} \quad 0\right]^T \quad (17)$$
$$r_k = \sqrt{x_k^2 + y_k^2 + z_k^2}$$

where μ is the Moon's gravitational parameter. An alternative option is to use a sequential filter such as an extended Kalman filter (EKF). Although these filters do not have the benefit of relinearization at a given epoch, they require fewer computational resources and estimate a given state with only that time instance's observations. An EKF may be useful for applications such as descent and ascent where the dynamics model may not be as simple as propagating an orbit and when dynamics change rapidly [39].

The batch processor in this analysis estimates LRS-1's position, velocity, and clock bias at epoch of January 14th, 2025 19:37:000 UTC and accumulates measurements over a three-hour interval when the LSS is in view (Figure 10). The batch iterates over the interval's measurements until converging to 10 cm of positioning error. It is important to note that two significant factors in batch processor performance are the batch analysis interval size and the modeled dynamics. This paper optimized the batch interval size to 3 hours to achieve the best OD performance.

Figure 10. Access count of the GPS to LRS and GPS to LSS over the 3 hour analysis interval.

11

However, for OD at a different epoch, a different interval size may improve performance. In addition, the simulation only assumes simple two-body dynamics for the LRS. Future work includes modeling the three-body Earth-Moon system with additional perturbations to further improve the batch processor.

Modeled Errors in Trilateration– Simulated errors on the Earth-based GPS measurements at lunar distances include receiver, transmitter, timing, and ephemeris errors. This analysis does not include Earth-based atmospheric effects; these are relieved through the 1000 km atmospheric mask above the Earth's surface.

Reference frame conversions between Earth-centered and Moon-centered frames may lead to additional errors. Orbit determination of the LRS requires accurate knowledge of both the GPS constellation orbit (provided in an Earth-centered frame) and of the LSS position (provided in a Moon-centered frame). Therefore, an estimate of the LRS orbit includes errors in position, velocity, and orientation modeling of the Earth and Moon system. Current models of the Earth and Moon are extremely accurate, resulting in a 1.3 cm residual in predicted vs. measured range between an Earth-based ground station and a retroreflector on the lunar surface [40]. This residual includes modeling errors in positioning, velocity, and rotation of the Moon and rotation of the Earth. Our simulation utilizes the DE440 model referenced in [40], which models the Moon and earth system out to year 2650. With the relatively close epoch of 2025 chosen in this analysis, we do not expect the residuals to grow significantly until then. Ultimately, reference frame errors are well beneath the noise floor of this analysis and are deemed negligible.

Pseudorange errors include modeling errors for both the GPS constellation and the LSS position, and biases and drift in the LRS's and the LSS's clock (Table 6). This analysis assumes both the LSS and LRS deploy the DSAC-FO. The LSS clock is bound by the time synchronization process described in previous sections, but the LRS's clock is free running. The simulation models a clock bias and drift for both the LSS and the LRS but assumes both have completed initial time-synchronization (Table 6). The simulation models errors as:

$$\varepsilon_k = \Gamma_k(b_0, \dot{b}) + \omega_k \qquad (18)$$

where the $\Gamma_k()$ operator produces random walk motion with a given initial bias and drift rate:

$$\Gamma_k(b_0, \dot{b}) = \Gamma_{k-1}(b_0, \dot{b}) + \dot{b}(t_k - t_{k-1}) \qquad (19)$$
$$\Gamma_0(b_0, \dot{b}) = b_0$$

and ω_k is zero mean Gaussian noise. The initial bias b_0 is determined at the start of the simulation as a uniform random variable ranging from $-b_m$ to b_m, where b_m is the modeled bias described in Table 6.

Table 6. Modeled Errors in Navigation Simulation

|	Error	Bias	Drift Rate	Noise 1σ
LRS	Clock Model	0.21 m (0.7 ns)	2.99e-6 m/s (1.0e-4 ns/s)	0.09 m (0.30 ns)
	Misc Receiver [41]	0.1 m	N/A	0.1 m
LSS	Per Axis Position Knowledge	1 m	0.1 m/hr	N/A
	Per Axis Velocity Knowledge	1 mm/s	0.1 mm/s/hr	N/A
	Timing Knowledge	0.81 m (2.7 ns)	4.23e-5 m/s (14.1e-5 ns/s)	0.47 m (1.56 ns)
	Misc Receiver [41]	0.1 m	N/A	0.1 m
GPS	Per Axis Position Knowledge	5 m	1 m/hr	N/A
	Per Axis Velocity Knowledge	1 mm/s	0.1 mm/s/hr	N/A
	Timing Knowledge	5 ns	N/A	1 ns
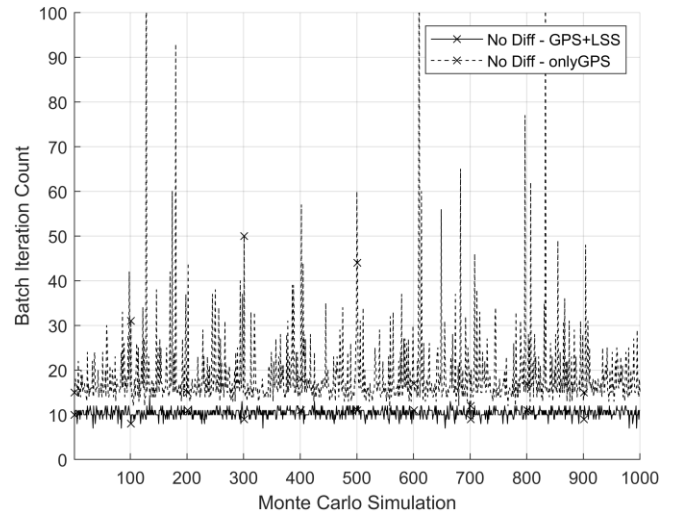
Figure 11. Batch processor iteration count over MC.

Simulation Parameters– The pseudorange measurement sampling rate for both the GPS constellation and the LSS is 1/60 Hz, or 1 measurement instance per minute. At each measurement instance, the user receives a pseudorange measurement from each GPS satellite in view along with the LSS, if it is in view. These measurements accumulate for use by the batch processor over the 3-hour analysis period.

A Monte Carlo (MC) simulation repeats the batch processor with new errors for all measurements over 1000 simulations to create a distribution of performance.

12

Table 7. 95% Confidence of Position, Velocity, and Timing Errors over 1000 Simulations (3 hours)

	Error	Per Axis	3D	Mean	Std
Only GPS	Position (m)	R: 168.4 A: 1044.8 C: 641.6	1173.8	518.4	363.8
	Velocity (mm/s)	R: 66.36 A: 95.72 C: 89.98	135.85	61.35	39.33
	Timing (ns)		2829.0	1152.8	970.9
GPS + LSS	Position (m)	R: 74.0 A: 74.8 C: 152.0	157.6	83.1	41.7
	Velocity (mm/s)	R: 5.54 A: 6.14 C: 17.49	15.36	7.23	4.15
	Timing (ns)		262.6	114.3	81.9
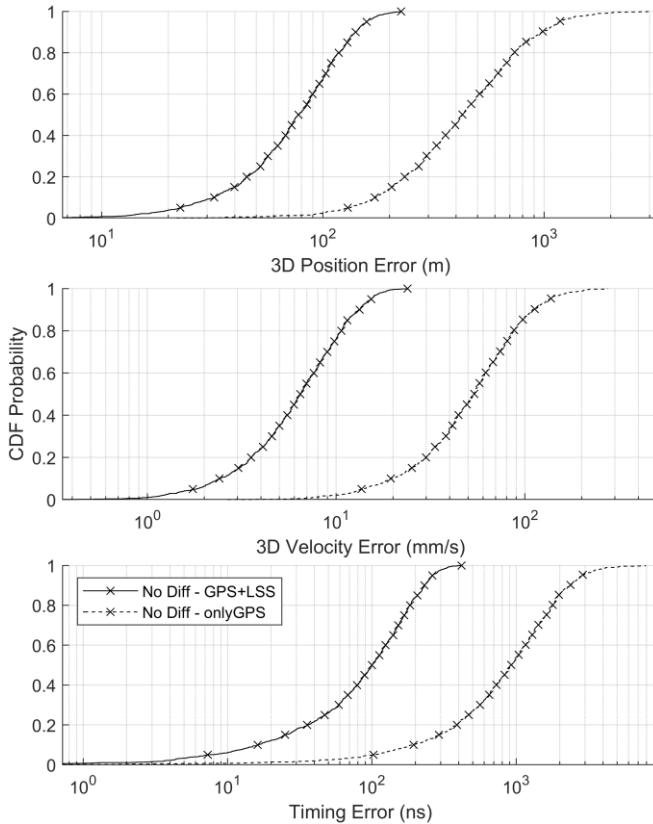
Figure 12. CDF of position, velocity, and timing performance of the batch processor over 3 hours.

Batch Results– Figure 11 depicts the batch iteration count over the 3-hour batch analysis interval. The batch processor converges at approximately 10 iterations with the use of the LSS measurement. With no LSS measurement and only Earth-based GPS signals, the batch iteration count averages just under 20 iterations with spikes up to the maximum of 100 iterations due to poor trilateration geometry. Table 7 describes the 95% confidence interval of the 3D position, velocity, and timing error of the estimated epoch state by the batch processor. Per axis errors are provided in the radial (R), along-track (A), and cross-track (C) reference frame at the epoch of the LRS orbit. Figure 12 depicts the cumulative density function (CDF) of the PVT performance, showing the significant improvement in accuracy with the LSS as a navigation node. Note that "No Diff" states that there are no differential corrections being applied to these methods.

Estimation performance of all states improve by around an order of magnitude when utilizing range measurements from the LSS. This large improvement is as expected; the DOP improvement with the LSS is around an order of magnitude as well (Figure 9). This demonstrates the significant benefit in geometry that a GPS transmitting LSS provides to an Earth-based GPS trilateration solution.

Ultimately, the addition of just a single surface station at the lunar south pole allows for an order of magnitude improvement in OD performance for lunar orbiters utilizing Earth-based GPS measurements.

6. DIFFERENTIAL GNSS RECEIVER ON THE LUNAR SURFACE

We assume that the LSS not only broadcasts a ranging code to the LRS constellation, but also communicates with the LRS to enable relay capabilities. This presents the opportunity for the LSS to also send range corrections to the LRS constellation. On Earth, differential GPS (DGPS) methods enable significant improvements in positioning accuracy of users through radiometric corrections from a nearby, well-known reference station [42]. DGPS takes advantage of the fact that both the user and reference station experience similar measurement errors which can be removed through measurement differencing. Because both the LRS and LSS can utilize Earth-based GPS measurements, a similar differential method can be deployed to improve OD.

Differential Methods

The differential methods used in this analysis are single and double measurement differencing. These methods not only reduce the shared errors between the LRS and LSS, but also receiver specific errors such as clock bias.

Single Differencing (SD)– This method differences the range measurement received at the LSS by the predicted measurement calculated from the station's well-known position. Assuming the station makes a code-based range measurement with a GPS satellite [43] [44]:

$$\rho_{LSS,k}^{(i)} = \rho_{LSS,k}^{(i)}\big|_{true} + c\big(\delta t_{LSS} + \omega_{\delta t_{LSS,k}}\big) \qquad (20)$$
$$+ c\left(\delta t_{GPS}^{(i)} + \omega_{\delta t_{GPS,k}}^{(i)}\right) + \varepsilon_{\rho_{LSS,k}} + \varepsilon_{\rho_{GPS,k}}^{(i)}$$

where δt_{LSS} and $\delta t_{GPS}^{(i)}$ are the clock biases, $\omega_{\delta t_{LSS,k}}$ and $\omega_{\delta t_{GPS,k}}^{(i)}$ are the clock noises, and $\varepsilon_{\rho_{LSS,k}}$ and $\varepsilon_{\rho_{GPS,k}}^{(i)}$ are the unique receiver and transmitter error terms for the LSS and

ith GPS satellite, respectively. Because the station knows its position with high accuracy, it can predict and difference the range measurement expected from the same satellite $\tilde{\rho}_{LSS,k}^{(i)}$:

$$\rho_{LSS,k}^{(i)} - \tilde{\rho}_{LSS,k}^{(i)} = c\left(\delta t_{LSS} + \omega_{\delta t_{LSS,k}}\right) \qquad (21)$$
$$+ c\left(\delta t_{GPS}^{(i)} + \omega_{\delta t_{GPS,k}}^{(i)}\right) + \varepsilon_{\rho_{LSS,k}} + \varepsilon_{\rho_{GPS,k}}^{(i)} + \varepsilon_{\rho_{SD}}^{(i)}$$
$$= \nabla\rho_{LSS,k}^{(i)}$$

where $\varepsilon_{\rho_{SD}}^{(i)}$ is the resulting error from the differencing operation. This resulting correction includes errors on the LSS range measurement. The station can then transmit this correction term to the LRS, which corrects its pseudorange measurement with the same satellite:

$$\rho_{LRS,k}^{(i)} = \rho_{LRS,k}^{(i)}|_{true} + c\left(\delta t_{LRS} + \omega_{\delta t_{LRS,k}}\right) \qquad (22)$$
$$+ c\left(\delta t_{GPS}^{(i)} + \omega_{\delta t_{GPS,k}}^{(i)}\right) + \varepsilon_{\rho_{LRS,k}} + \varepsilon_{\rho_{GPS,k}}^{(i)}$$
$$\rho_{LRS,k}^{(i)} - \nabla\rho_{LSS,k}^{(i)} = \rho_{LRS,k}^{(i)}|_{true} + c\left(\delta t_{LRS} + \omega_{\delta t_{LRS,k}}\right) + \varepsilon_{\rho_{LRS,k}}$$
$$+ c\left(\delta t_{LSS} + \omega_{\delta t_{LSS,k}}\right) + \varepsilon_{\rho_{LSS,k}} + \varepsilon_{\rho_{SD}}^{(i)}$$
$$\rho_{LRS,k}^{(i)\,SD} = \rho_{LRS,k}^{(i)} - \nabla\rho_{LSS,k}^{(i)}$$

This results in the reduction of shared error between the LRS and LSS: the satellite clock and transmitting errors. Although not included in these simplified measurement models, the SD method can also reduce shared atmospheric and deep space delays. Because the GPS signals to both the LSS and LRS experience very similar flight paths, any additional delays on the radiometric measurements are encompassed by the station's SD correction term.

Double Differencing (DD)– The DD method differences two SD measurements to further remove errors on the user's radiometric measurement. Now, DD requires two satellites to be in view by both the LRS and LSS. The SD measurements from satellites i and j can be differenced to remove receiver specific errors:

$$\rho_{LRS,k}^{(i)\,SD} - \rho_{LRS,k}^{(j)\,SD} = \rho_{LRS,k}^{(i)}|_{true} - \rho_{LRS,k}^{(j)}|_{true} \qquad (23)$$
$$+ \varepsilon_{\rho_{SD}}^{(i)} - \varepsilon_{\rho_{SD}}^{(j)} + \varepsilon_{\rho_{DD}}^{(ij)}$$

where $\varepsilon_{\rho_{DD}}^{(ij)}$ is error that cannot be removed through DD. This DD measurement now reduces user and station specific receiver errors such as clock bias and noise. This is especially useful when the user's clock errors are significant.

Another benefit of DD relative to SD is how the number of measurements scale with the number of satellites in view. The observable count for standard and SD-corrected trilateration scales directly proportional to the number of satellites in view. However, because DD differences a pair of satellite measurements, the observation count increases with the number of unique pairs of satellites in view (Figure 13). For instance, if there are 5 satellites in view, there are ten
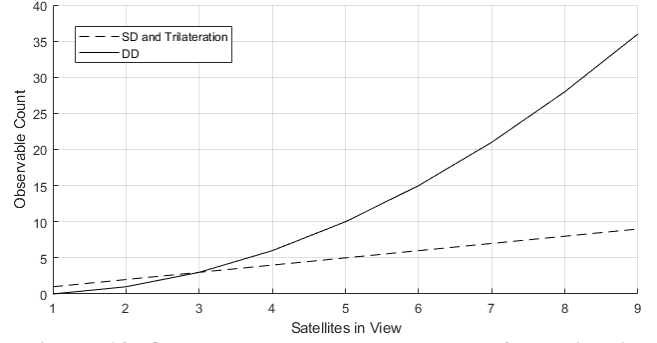

Figure 13. Observable count vs. number of satellites in view for SD and DD.

unique pairs of satellites and 10 DD observables. This increases observability during the batch process.

Both SD and DD provide valuable improvements to radiometric measurements but also increase requirements and complexity. Along the well-known reference station can transmit radiometric corrections, the user must align these corrections with their own measurements in time. A misalignment of correction and measurement can lead to additional errors that grow as a function of the misalignment duration [14]. This analysis assumes that the LSS transmits corrections at a high rate with additional instructions on interpolation of the corrections in time. The user can then align the correction with their respective measurements without significant time misalignment.

Previous studies analyzed the benefits of SD and DD in lunar navigation settings [39] [43] [44] with a brief analysis on orbit determination with DD [14]. However, we analyze the use of SD and DD on Earth-based GPS measurements at lunar distances.

Orbit Determination with LSS-Aided Differential GPS

This analysis repeats the navigation simulation in Section 4 but now with the addition of SD and DD corrections from the LSS. The LSS receives Earth-based GPS measurements over an elevation mask of 0 degrees (approximately 1 deg from the terrain horizon in Figure 1). Separate batch processors accumulate SD and DD measurements for comparison.

Simulation Parameters– The measurement sampling rate and measurement error generation statistics remain the same from the simulation in Section 4. However, there are additional considerations for the measurement differencing methods. 1) if the number of satellites in view by both the LRS and LSS ever drops under two, then DD is not possible. Thus, the DD method reverts to SD until two or more satellites are visible. 2) if the LRS and LSS do not have access to the same satellite, or 3) if the LRS no longer has access to the LSS, the simulation returns to standard pseudorange measurements without measurement differencing. Although these conditions do not apply for this analysis's 3-hour interval, they are important considerations for implementation.

14

Table 8. SD and DD 95% Confidence of Position, Velocity, and Timing Errors over 1000 Simulations

		Error	Per Axis	3D	Mean	Std
SD Corrections from LSS	**Only GPS**	Position (m)	R: 21.3 A: 88.0 C: 42.7	103.6	41.9	32.4
		Velocity (mm/s)	R: 5.01 A: 5.02 C: 6.25	9.02	3.69	2.73
		Timing (ns)		288.3	113.8	92.0
	GPS + LSS	Position (m)	R: 2.8 A: 5.5 C: 8.2	8.9	4.5	2.3
		Velocity (mm/s)	R: 0.23 A: 0.45 C: 0.66	0.63	0.34	0.17
		Timing (ns)		16.4	6.8	5.1
DD Corrections from LSS	**Only GPS**	Position (m)	R: 27.9 A: 40.9 C: 19.2	65.9	25.4	21.2
		Velocity (mm/s)	R: 2.18 A: 0.88 C: 1.85	3.28	1.34	0.99
		Timing (ns)		219.2	84.9	72.7
	GPS + LSS	Position (m)	R: 1.7 A: 2.9 C: 3.1	3.8	2.2	0.9
		Velocity (mm/s)	R: 0.14 A: 0.25 C: 0.45	0.44	0.22	0.12
		Timing (ns)		13.5	5.7	4.2

Figure 14. CDF of position, velocity, and timing performance of the batch processor over with SD and DD corrections from LSS.

As with the previous analysis, an MC repeats the batch processor for 1000 simulations.

Results– Table 8 depicts the 95% confidence values of the distribution of PVT performance of the SD and DD batch estimators. SD corrections reduce errors from the results in Table 7 by another order of magnitude due to the removal of shared GPS transmitter and timing errors. DD further reduces errors from SD by around a factor of two or less by also mitigating LSS and LRS specific receiver and timing errors, resulting in RSS position errors of <4 m at 95% confidence.

There is a significant overlap between the CDFs of SD and DD in the cases with and without the use of LSS-based GPS range measurements. For instance, if SD measurements and the LSS ranging code are available, but DD corrections are unavailable, it is better to use SD with LSS-based GPS measurements than DD without the LSS measurements. Not using any differential corrections, however, always results in worse PVT performance. Thus, differential corrections from the LSS should be used when possible.
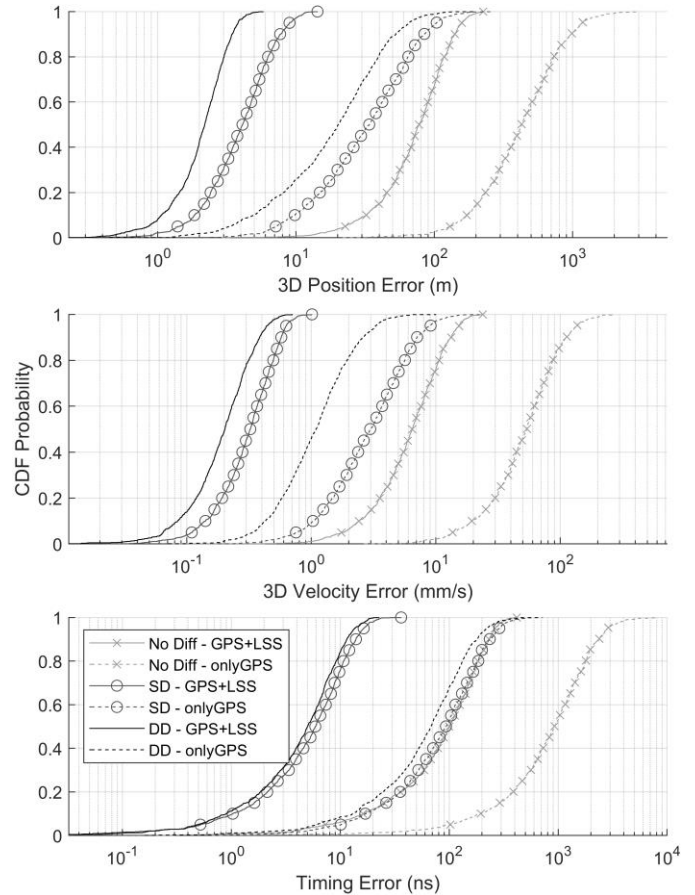
Although distinctions in performance between the configurations are obvious for position and velocity estimation, timing estimation is more unclear. DD and SD with LSS measurements provide the best timing estimation performance while DD without LSS, SD without LSS, and No Diff with LSS all provide similar performance. This may be a result of the significant improvement in timing geometry by the LSS, and marginal improvement in timing estimation between SD and DD.

These results include configurations where the LRS can receive differential corrections from the LSS, but not range measurements from the LSS. This is not an unlikely occurrence; the LSS could be relaying communications data instead of broadcasting a ranging code to the LRS while also embedding Earth-based GPS measurement correction data in the communications packets. When no communication relay services are needed, the LSS can return to broadcasting ranging codes for improved LSS OD performance.

15

7. LOCAL SURFACE USER POSITIONING

Radiometric corrections from the LSS are not only useful for OD of the LRS constellation. In-situ, one-way radiometric measurements broadcasted from the LRS constellation to surface users near the lunar south pole can be further improved with corrections sent from the LSS.

Previous analyses with JDR discuss real-time PVT estimation for lunar surface users with the use of DD-JDR, a well-known LSS, and a three-satellite navigation constellation [45]. With this navigation architecture, DD-JDR achieved <10 m, 17 mm/s, and 230 ns of position, velocity, and timing error at 95% confidence for a highly accelerating surface user. Repeating this analysis for real-time PVT of an orbiting user results in 25 m, 0.8 m/s, and 230 ns of PVT error at 95% confidence with only in-situ measurements [14]. An important note is that these analyses assumed autonomous orbit determination for their LRS constellations, resulting in large orbit ephemeris modeling errors: 100 m positioning biases per axis. Using this paper's method of orbit determination with measurement differencing and Earth-based GPS measurements would lead to improved orbiter modeling, resulting in improved surface navigation performance. For instance, a parallel paper implements DD-JDR for PVT estimation onboard a simulated lunar lander, resulting in <10 m, 0.45 m/s, and 340 ns PVT performance at 3-sigma (99.73%) confidence [46], assuming the LRS constellation modeling knowledge mimics the results describe in this paper.

A previous DD-JDR analysis assumed 10 ns biases for the LRS constellation [45], which is close to the timing estimation performance of SD and DD with LSS range measurements (Table 8). In addition, if a preemptive time synchronization with the LSS is possible, the LRS timing error can be even lower (Table 3). For surface positioning with an in-situ navigation system, the relative time synchronization between the LSS and LRS constellation is more important. Thus, lunar surface users will estimate their clock biases relative to a lunar navigation time. Assuming that the lunar navigation time is frequently synchronized to GPS time through the DSN to LSS link, the conversion between lunar and GPS time will be known. However, during the ~2 week interval when Earth is not in view to the LSS, the lunar navigation time, led by the LSS, may drift from GPS time. If in-situ time synchronization is performed periodically (between LSS and LRS constellation) a margin of drift of the lunar navigation time may be acceptable during in-situ surface user navigation services.

As discussed in Section 4, the navigation architecture will need to be carefully designed to reduce the potential of interference. The LRS constellation is expected to broadcast PRN codes to the lunar south pole in S-band, offset in frequency from the LSS's broadcast up to the LRS constellation. In addition, the LSS will broadcast corrections and another PRN code in UHF to its local region near the Connecting Ridge. This allows surface users to continuously receive two to three Doppler and pseudorange measurements from the constellation, one pseudorange measurement from the LSS, and corrections on the LRS radiometric measurements from the LSS.

8. CONCLUSIONS AND FUTURE IMPACTS

This paper introduces a lunar surface PNT architecture that provides the following functions: a) provides time distribution services to orbiting and surface spacecraft, b) supports OD of orbiting assets, and c) augments a lunar relay network to provide precision PNT services for surface assets. We describe the operations and perform extensive simulations to quantify the performance of a ground-assisted PNT architecture for the Moon.

In addition, the ground-assisted PNT architecture also supports NASA's "Moon-to-Mars" initiative. The "Moon-to-Mars" initiative refers to a long-term overarching exploration strategy, which involves human missions to the Moon as a steppingstone for crewed missions to Mars. The plan is to use the Moon as a testbed for technologies, systems, and operations necessary for human missions to Mars. By establishing a sustainable presence on the Moon, NASA aims to gain valuable experience and knowledge that will help in preparing for crewed missions to the Red Planet.

While the Moon-to-Mars approach is a logical and sound strategy, we must also recognize the differences between the Moon and Mars and adjust the strategy accordingly. The Moon is less than 400,000 km from Earth, whereas Mars is between 75 million km and 400 million km. The difference in range results in the following:

- Unlike lunar spacecraft, Mars spacecraft cannot receive Earth's GPS and GNSS signals. Mars relay orbiters would have to rely on either the Earth's deep space ground antennas, or a local Mars frequency and timing reference to perform orbit determination. The latter would relieve the burden on the Earth's ground antenna infrastructures and provide additional in-situ PNT capabilities for Mars orbiters and surface assets.

- The one-way-light-time delay with Mars is between 4 minutes to 20 minutes, thus real-time communications with Earth is not possible. Mars spacecraft cannot rely on Earth for real-time commanding and must be more autonomous in responding to unexpected and off-nominal situations. Therefore, autonomy and real-time kinematic PNT during spacecraft dynamic events are more relevant for Mars than for Moon.

- It is more costly to send orbiting and surface spacecraft to Mars than to the Moon.

There is also a big difference in the rotation rates. A Mars day is 24 hours and 37 minutes, and a lunar day is about 27.3 Earth days.

16

Differences in regions of interest on the Moon and Mars surface also dictate mission requirements. Early human exploration of the Moon will focus on the lunar south pole, and this presents a unique and challenging operation environment in terms of Earth and relay communications, sun illumination, and thermal variation. To provide maximum coverage, the proposed lunar relay constellations favor frozen elliptical orbits that loiter above the lunar south pole. Due to the Earth-Moon geometry and long lunar night because of tidal-locking, many regions at the lunar south pole do not see Earth for an extended period in each lunar cycle. Also, Earth and the Sun appear at low-elevation angles as viewed from the lunar south pole. Even in view, direct communication with Earth suffers from high multipath loss. The combination of low grazing angle of sunlight, absence of an atmosphere, and low rotation rate results in large thermal variations and extremely low temperature in some parts of the lunar south pole. The extreme thermal environment requires that the communications and PNT equipment on the lunar surface to be housed inside a temperature-controlled vault, and this imposes tight requirements on SWaP.

Human exploration of Mars, on the other hand, focuses on the equatorial and mid-latitude regions. Most proposed relay network designs favor circular equatorial orbits. The sun illumination and thermal environments are more benign. However, Mars has a thin atmosphere, and the occasional sandstorms can pose different kinds of challenges to communications and navigation on the Mars surface.

Although a Martian surface station could provide many of the same benefits described in this paper, we cannot assume the results in this paper are directly applicable to human Mars exploration. Holistic system engineering studies and architecture trades are needed to identify the differences between the lunar and Mars operation scenarios, to understand the inter-dependency between engineering systems and the environments, and to adapt and adjust the "Moon-to-Mars" strategy accordingly.

ACKNOWLEDGEMENTS

REFERENCES

[1] D. J. Israel, N. Babu, "Draft LunaNet Interoperability Specification", NASA/TP–20210021073/Rev.3. 2022

[2] P. Gläser, et. al., "Illumination conditions at the lunar poles: Implications for future exploration", Planetary and Space Science, 162, 2018

[3] P. Gläser, et. al. "Temperature Near the Lunar Poles and Their Correlation with Hydrogen Predicted by LEND," Journal of Geophysical Research: Planets, 126:9, 2021

[4] K. Bhasin et. al. "Lunar Communication Terminals for NASA Exploration Missions: Needs, Operation Concepts, and Architectures," AIAA ICSSC Conference, June 2008.

[5] S. Oleson, M. McGuire, "COMPASS Final Report: Lunar Satellite-High Rate (LNS-HR)", NASA/TM—2012-217139, July 2012

[6] Nokia Bell Labs, "The First Cellular Network on the Moon", https://www.bell-labs.com/research-innovation/network-fundamentals/first-cellular-network-on-the-moon/#gref

[7] S. Bhamidipati, T. Mina, and G. Gao, "A Case Study Analysis for Designing a Lunar Navigation Satellite System with Time Transfer from the Earth GPS," NAVIGATION: Journal of the Institute of Navigation, vol. 70, no. 4, p. navi.599, 2023, doi: 10.33012/navi.599.

[8] S. Bhamidipati, T. Mina, and G. Gao, "Time Transfer from GPS for Designing a SmallSat-Based Lunar Navigation Satellite System," NAVIGATION: Journal of the Institute of Navigation, vol. 69, no. 3, p. navi.535, 2022, doi: 10.33012/navi.535.

[9] L. Winternitz et. al. "GPS Based Autonomous Navigation Study for the Lunar Gateway," AAS Guidance & Control Conference, Breckenridge, CO., 2019

[10] J. Small et. al., "Lunar Relay Onboard Navigation Performance and Effects on Lander Descent to Surface," 2022 International Technical Meeting of the Institute of Navigation, February 2022.

[11] S. J. Boazman, et. al., "The Distribution and Accessibility of Geologic Targets near the Lunar South Pole and Candidate Artemis Landing Sites", The Planetary Science Journal, 3:275, 2022

[12] NASA, "NASA's Plan for Sustained Lunar Exploration and Development", NASA Artemis Program 2020, https://www.nasa.gov/sites/default/files/atoms/files/a_sustained_lunar_presence_nspc_report4220final.pdf

[13] K. Cheung, et. al. "Single-Satellite Real-Time Relative Positioning for Moon and Mars," IAC, Washington DC., 2019

[14] W. W. Jun, "Performance of a Low Infrastructure Navigation System for Planetary Surface Users", Doctoral thesis, School of Aerospace Engineering, Georgia Institute of Technology, 2023

[15] W. W. Jun, K. M. Cheung, E. G. Lightsey, C. Lee, "A Minimal Architecture for Real-Time Lunar Surface Positioning using Joint Doppler and Ranging," IEEE Transactions on Aerospace and Electronic Systems, 58:2, 2022

[16] NASA, "Explore Moon to Mars", https://www.nasa.gov/topics/moon-to-mars

[17] S. R. Oleson, M. L. McGuire. "COMPASS Final Report: Lunar Communications Terminal (LCT)", Glenn Research Center, NASA/TM-2010-216236, https://ntrs.nasa.gov/api/citations/20110004245/downloads/20110004245.pdf

[18] F. Vannicola, R. Beard, J. White, K. Senior, M. Largay, J. Buisson, "GPS Block IIF Atomic Frequency Standard Analysis", 42nd Annual Precise Time and Time Interval (PTTI) Meeting, 2010

[19] Wu, A., Feess, B., 2000. Development and evaluation of GPS space clocks for GPS III and beyond. In: 32nd Annual Precise Time and Time Interval (PTTI) Meeting. pp. 389–399.

[20] P. Steigenberger, S. Thoelert, O. Montenbruck, "GPS III Vespucci: Results of half a year in orbit", Advances in Space Research, 66:12, 2020

[21] Lockheed Martin, "GPS III/IIIF The New Generation of Positioning Navigation and Timing", 2023, https://www.lockheedmartin.com/en-us/products/gps.html

[22] Burt, E.A., Prestage, J.D., Tjoelker, R.L. et al. "Demonstration of a trapped-ion atomic clock in space", Nature 595, 43–47, 2021

[23] S. Smrekar, et. al. "VERITAS (Venus Emissivity, Radio Science, InSAR, Topography, and Spectroscopy): A Selected Discovery Mission," IEEE Aerospace Conference, Big Sky, MT, March 2022.

[24] Hoang, T.M., Chung, S.K., Le, T. et al. "Micro mercury trapped ion clock prototypes with $10-14$ frequency stability in 1-liter packages," Sci Rep 13, 10629, 2023, doi: 10.1038/s41598-023-36411-x

[25] L. B. Winterntiz, W. A. Bamford, A. C. Long, M. Hassouneh, "GPS Based Autonomous Navigation Study for the Lunar Gateway", AAS GNC, 2019

[26] Y. Kim and H. Bang, "Introduction to Kalman Filter and Its Applications," Introduction and Implementations of the Kalman Filter, May 2019, doi: 10.5772/intechopen.80600.

[27] T. Krawinkel and S. Schön, "Benefits of receiver clock modeling in code-based GNSS navigation," GPS Solutions, vol. 20, no. 4, pp. 687–701, Aug. 2015, doi: 10.1007/s10291-015-0480-2.

[28] C. Zucca and P. Tavella, "The clock model and its relationship with the Allan and related variances," IEEE Transactions on Ultrasonics, Ferroelectrics and Frequency Control, vol. 52, no. 2, pp. 289–296, Feb. 2005, doi: 10.1109/tuffc.2005.1406554.

[29] S. Srinivas, A. Herschfelt, D. W. Bliss, "Extended Kalman Filter Design for Tracking Time-of-Flight and Clock Offsets in a Two-Way Ranging System," Signals, 4:2, 2023, doi: 10.3390/signals4020023

[30] Y. Mo, X. Deng, L. Zheng, Z. Liu, "Kalman-consensus filter for time synchronization in wireless sensor networks," IET International Conference on Information and Communications Technologies, 2013, doi: 10.1049/cp.2013.0080

[31] H. Monaghen, "What is the Deep Space Network?" NASA, Mar 2020, [Online], Available: https://www.nasa.gov/directorates/heo/scan/services/networks/deep_space_network/about

[32] C. Chang, "810-005 Deep Space Network (DSN) Telecommunications Link Design Handbook", 001, Rev. B Handbook Introduction, NASA JPL, 2011, [Online], Available: https://deepspace.jpl.nasa.gov/dsndocs/810-005/001/001B.pdf

[33] J. Betz. "Link Budgets", International Committee on GNSS Working Group A. Torino, Italy, 2010

[34] T. Anthony. "NAVSTAR GPS Space Segment/Navigation User Segment Interfaces", Gps.gov, 2022.

[35] T. Qin, D. Qiao, M. Macdonald, "Relative orbit determination using only intersatellite range measurements," The Journal of Guidance, Control, and Dynamics, 42:3, 2019.

[36] L. Singh, S. Lim, "On lunar on-orbit vision-based navigation: Terrain mapping, feature tracking driven EKF," AIAA Guidance, Navigation and Control Conference and Exhibit, Honolulu, HI, 2008

[37] F. Daum. "Nonlinear filters: beyond the Kalman filter", IEEE Aerospace and Electronics Systems Magazine, 2005

[38] B. D. Tapley, B. E. Schutz, G. H. Born, "Statistical Orbit Determination", Academic Press, 2004

[39] W. W. Jun, K-M. Cheung, E. G. Lightsey, "Positioning, Navigation, and Timing for Lunar Descent and Landing with Joint Doppler and Ranging", IEEE Aerospace Conference, 2024.

[40] R. S. Park, W. M. Folkner, J. G. Williams, D. H. Boggs, "The JPL Planetary and Lunar Ephemerides DE440 and DE441", The Astronomical Journal, 161:105, 2021

[41] E. D. Kaplan, C. J. Hegarty, "Understanding GPS Principles and Applications Second Edition", Artech House, 2006

[42] P. Misra, P. Enge, "Global Positioning System: Signals, Measurements, and Performance," 2nd Edition, Ganga-Jamuna Press, 2012

[43] W. W. Jun, K-M. Cheung, E. G. Lightsey, "Frequency Bias Mitigation for Surface User Navigation using Double Differencing Joint Doppler and Ranging", IEEE Transactions on Aerospace and Electronic Systems. Preprint at: https://sites.gatech.edu/wwjpublications

[44] W. W. Jun, K-M. Cheung, E. G. Lightsey, "Improved Surface Positioning with Measurement Differences in Joint Doppler and Ranging", Proceedings of the 2023 IEEE Aerospace Conference, Big Sky, Montana, 2023

[45] W. W. Jun, K-M. Cheung, E. G. Lightsey, "Real-Time Position, Velocity, and Timing Estimation of Lunar Surface Users with Joint Doppler and Ranging", IEEE Transactions on Aerospace and Electronic Systems. Preprint at: https://sites.gatech.edu/wwjpublications

[46] W. W. Jun, K-M. Cheung, E. G. Lightsey, "Position, Velocity, and Timing for Lunar Descent and Landing with Joint Doppler and Ranging", Proceedings of the 2024 IEEE Aerospace Conference, Big Sky, Montana, 2024

BIOGRAPHY

Kar-Ming Cheung received the B.S.E.E. degree from the University of Michigan, Ann Arbor, in 1984, and the M.S. and Ph.D. degrees from California Institute of Technology in 1985 and 1987, respectively. He is a Principal Engineer and Technical Group Supervisor in the Communication Architectures and Research Section (332) at JPL. His group supports design and specification of future deep-space and near-Earth communication systems and architectures. Since 1987, he has been with JPL where he is involved in research, development, production, operation, and management of advanced channel coding, source coding, synchronization, image restoration, and communication analysis schemes. Dr. Cheung received NASA's Exceptional Service Medal for his work on Galileo's onboard image compression scheme.

William W. Jun received his B.S., M.S., and Ph.D. degrees in aerospace engineering from the Georgia Institute of Technology in Atlanta, Georgia in 2018, 2020, and 2023 respectively. He is currently a Telecommunications Engineer at NASA Jet Propulsion Laboratory (JPL). During his stay at Georgia Tech, he worked in the Space Systems Design Laboratory (SSDL) on various CubeSat missions as subsystem leads and as the Project Manager of Prox-1. He was a Research Fellow at NASA JPL in the summers of 2018 to 2023. His research interests include navigation architectures, navigation methods, and estimation techniques. He was a recipient of the NASA Space Technology Research Fellowship in 2019.

Sriramya Bhamidipati received her Ph.D. in Aerospace Engineering at the University of Illinois, Urbana-Champaign in 2021, where she also received her M.S in 2017. She obtained her B.Tech. in Aerospace from the Indian Institute of Technology, Bombay in 2015. She is currently a robotics technologist in the maritime and multi-agent autonomy group at NASA JPL. Her research interests include GPS, computer vision, unmanned aerial vehicles and space robotics. Before joining JPL, she worked as a postdoctoral scholar in the navigation and autonomous vehicles lab at Stanford University. She received the Amelia Earhart Fellowship in 2020 and was awarded best presentation at ION GNSS+ four times in 2016, 2017, 2021 and 2022.

Paul Carter received his B.S. and M.S. degrees in Aerospace Engineering from the Georgia Institute of Technology in 2021 and 2023 respectively. During both his undergraduate and graduate years, he was a member of the Georgia Tech Space Systems Design Laboratory (SSDL). While there, he worked on CubeSat missions and started his research on deep space relay architectures. He is now working full time as a Telecommunications Engineer at NASA Jet Propulsion Laboratory (JPL).